Supporting information for:

Revealing the Synergistic Effect of Ni Single Atoms and Adjacent 3d metal Doped Ni Nanoparticles in Electrocatalytic CO_2 Reduction

Yingjie Liu,[a,†] Zhaohui Wu,[a,†] Sha Bai,[a] Tianyang Shen,[a] Qian Li,[a] Guihao Liu,[a] Xiaoliang Sun,[a] Yihang Hu,[a] Ziheng Song,[a] Jinfeng Chu,[a,*] and Yu-Fei Song [a,b*]

[a]State Key Laboratory of Chemical Resource Engineering, Beijing University of Chemical Technology, Beijing 100029 P. R. China.

[b]Quzhou Institute for Innovation in Resource Chemical Engineering, Quzhou, Zhejiang Province, 324000 P. R. China.

[†]These authors contributed equally to this work.

List of Contents:

Experimental Section

Figure S1. XRD patterns of NiMAl-LDH.

Figure S2. XRD patterns of $Ni_{1+NPs}M@NCNTs$.

Figure S3. Raman spectra of $Ni_{1+NPs}M@NCNT$.

Figure S4. (a-f) SEM images of $Ni_{1+NPs}M@NCNT$ (M=Mn, Fe, Co, Ni, Cu, Zn).

Figure S5. TEM images of (a) $Ni_{1+NPs}Mn@NCNT$ and (b) $Ni_{1+NPs}Fe@NCNT$.

Figure S6. EDX elemental mapping image of N in the $Ni_{1+NPs}Cu@NCNT$.

Figure S7. (a) STEM image of $Ni_{1+NPs}Cu@NCNT$ and (b) the corresponding STEM-EDX line scanning image.

Figure S8. EXAFS in k space of $Ni_{1+NPs}@NCNT$, $Ni_{1+NPs}Cu@NCNT$ and Ni foil.

Figure S9. Cu K-edge XANES spectra of $Ni_{1+NPs}Cu@NCNT$ and Cu foil

Figure S10. XPS of $Ni_{1+NPs}@NCNT$, $Ni_{1+NPs}Mn@NCNT$, $Ni_{1+NPs}Fe@NCNT$ and $Ni_{1+NPs}Cu@NCNT$.

Figure S11. (a) N 1s and (b) Ni 2p XPS spectra of $Ni_{1+NPs}@NCNT$, $Ni_{1+NPs}Mn@NCNT$, $Ni_{1+NPs}Fe@NCNT$ and $Ni_{1+NPs}Cu@NCNT$.

Table S1. EXAFS fitting results of $Ni_{1+NPs}Cu@NCNT$, $Ni_{1+NPs}@NCNT$ and Ni foil.

Figure S12. (a-f) LSV curves of $Ni_{1+NPs}M@NCNT$ under Ar (black) and CO_2 (colored) atmosphere.

Figure S13. Characterization for the liquid product of $Ni_{1+NPs}M@NCNT$ after the full-potential-CO_2RR period by ^1H nuclear magnetic resonance spectroscopy.

Figure S14. CO_2RR performance of $Ni_{1+NPs}M@NCNT$. (a) FE_{CO} of $Ni_{1+NPs}M@NCNT$ (M=Mn, Fe, Co, Ni, Cu, Zn); (b) contour plots of J_{CO} under different potential.

Table S2. FE_{CO} of $Ni_{1+NPs}M@NCNT$ under different potentials.

Figure S15. Typical cyclic voltammetry curves for (a) $Ni_{1+NPs}@NCNT$, (b) $Ni_{1+NPs}Mn@NCNT$, (c) $Ni_{1+NPs}Fe@NCNT$ and (d) $Ni_{1+NPs}Cu@NCNT$ under different scan rates.

Figure S16. (a) XRD patterns of $Ni_{1+NPs}Cu@NCNT$ before (black) and after (red) CO_2RR; (b) TEM image of the $Ni_{1+NPs}Cu@NCNT$ after CO_2RR.

Figure S17. DFT models for $Ni_{1+NPs}@NCNT$ and $Ni_{1+NPs}Cu@NCNT$.

Figure S18. CO_2RR performance of $Ni_{NPs}@NCNT$. (a) current density and (b) FE_{CO} and FE_{H2} under different potentials.

Figure S19. (a) Schematic illustration and (b) photograph of the flow cells.

Figure S20. (a) TCD1 Chromatogram of CO; and (b) TCD2 Chromatogram of H_2.

Table S3. Comparison of CO_2RR performance displayed by our catalyst and other reported works.

Experimental Section

Materials: $NiCl_2 \cdot 6H_2O$, $AlCl_3 \cdot 6H_2O$, $FeCl_3 \cdot 6H_2O$, $MnCl_2 \cdot 4H_2O$, $CoCl_2 \cdot 6H_2O$, $CuCl_2 \cdot 2H_2O$, $ZnCl_2$, NaOH, $KHCO_3$, melamine, HCl were purchased from Sigma-Aldrich Co. and were used without any further purification. Deionized water was used in all the experimental processes. Nafion 211 membrane was purchased from Dupont. Carbon dioxide (99.999%) was purchased at Beijing Beiwen Gas Comp.

Synthesis of NiMAl-LDH (X=Ni, Mn, Fe, Co, Cu, Zn): 47.5mmol $NiCl_2 \cdot 6H_2O$, 25mmol $AlCl_3 \cdot 6H_2O$ and 2.5mmol chloride of metal X were dispersed in 35 mL deionized water as solution A. NaOH and Na_2CO_3 were dispersed in another 50mL deionized water and added dropwise into solution A under 80°C. The obtained mixture was then stirred under 80°C for 12h and washed by deionized water till pH=7. The drying process finally gave rise to NiMAl-LDH.

Synthesis of $Ni_{1+NPs}M@NCNT$ (M= Ni, Mn, Fe, Co, Cu, Zn): 3g melamine and 50mg NiMAl-LDH were milled together to get well-mixed powder, which was then calcined in a tubular furnace under N_2 atmosphere at 650°C for 3h. The calcined product was then stirred in 3 mol L^{-1} HCl for 24h to remove the exposed nanoparticles and impurities. The sample was then washed by deionized water and dried.

Characterization: XRD patterns were collected by powder X-ray diffraction (XRD) on Bruker D8 diffractometer with Cu-Kα radiation (λ=1.5405 Å). Scanning electron microscopy (SEM) images were obtained utilizing a Zeiss Supra55. High-resolution transmission electron microscopy (HRTEM) images were performed on a FEI Talos F200x. Ni and Cu K-edge X-ray absorption fine structure (XAFS) measurements were performed at the 1W1B beamline of the Beijing Synchrotron Radiation Facility. Raman spectroscopy was performed at a Jobin-Yvon LabRam HR800 microscope. XPS spectra was calibrated against C 1s at 284.8 eV. The gas and liquid products were analyzed using Gas chromatography-mass spectrometry (GC-MS, QP2020 equipped with Micropacked column) and NMR (AVANCE III HD 400), respectively.

Electrochemical measurements: The measurements were taken in a H-type cell connected to an electrochemical station (CHI660A). Pt plate was chosen as the counter

electrode and the Ag/AgCl electrode served as reference electrode. The data was converted to those against the reversible hydrogen electrode (RHE) before analysis. For the working electrode, a typical procedure is to disperse 5mg sample and 10 μL Nafion solution in 1mL ethanol solution. Afterwards, 200 μL mixture was taken and loaded on the carbon fiber paper with the size of $1*2$ cm^2 in an area of $1*1$ cm^2. LSV test, CV test and the faradaic efficiency analysis were taken in 0.25M KHCO$_3$ after injection of CO$_2$ gas for 30 minutes, which remains at the flow rate of 20 mL/min during the entire catalytic period.

Faradic efficiency calculation: Faradic efficiency was calculated by the equation:

$$FE = \frac{n \times Z \times F}{Q} \times 100\%$$

n is the moles of the product; F is the Faradaic constant (96485.33289 C mol^{-1}); Z: the number of transferred electrons ($Z_{CO}=Z_{H2}= 2$); Q is the total charge calculated during CO$_2$RR.

$$n = \frac{P_0 \times v \times V}{R \times T}$$

P_0 is the standard atmospheric pressure (101.325 kPa); v is the gas flow rate (20 mL/min); V is the volume concentration of the calculated product in the outlet gas from the catalytic system; T is the reaction temperature (298 K) and R is the ideal gas constant (8.314 J mol^{-1} K^{-1}).

CO$_2$ electrolysis in flow cells: CO$_2$RR was taken in a flow cell equipped with gas diffusion electrodes (GDE), where Ag/AgCl electrode served as reference electrode. The catalyst ink was prepared in the same way and loaded on the carbon fiber paper with the size of 1×1 cm^2. KOH was chosen as the catholyte and anolyte, which were cycled at a flow rate of 14 mL min^{-1} by using a peristaltic pump.CO$_2$ gas flow was delivered into the gas chamber at 14 sccm and collected for GC analysis.

Computational details

All spin-polarized DFT calculations were performed using the QUICKSTEP module in the CP2K package (version 2023.1)[1]. The exchange-correlation potential in the single-electron Kohn-Sham equation was described by generalized gradient

approximation (GGA) with the Perdew-Burke-Ernzerhof (PBE) functional[2]. Wavefunctions were expanded in molecularly optimized (MOLOPT) double ζ-valence polarized basis set[3] with an auxiliary plane-wave basis set with a cutoff energy of 410 Ry. Core electrons were modeled by scalar relativistic norm-conserving Goedecker-Teter-Hutter (GTH) pseudopotentials[4] with 18, 11, 15, 16, 4, 5, 6, and 1 valence electrons for Ni, Cu, Mn, Fe, C, N, O, and H, respectively. Grimme's D3 method with Becke-Johnson (B-J) damping [5, 6] was added to study the impact of van der Waals interaction. The Monkhorst-Pack gamma centered 3×3×1 k point mesh was used for Brillouin zone sampling during geometry optimization process and self-consistent field (SCF) interaction was carried out with a conventional diagonalized method.

The density of state (DOS) was analyzed by Multiwfn package[7] with the formed molden file in single point calculation. The projected DOS (pDOS) was calculated with the C-Squared Population Analysis (SCPA) method[8] and the Gaussian function was selected to be the broadening function.
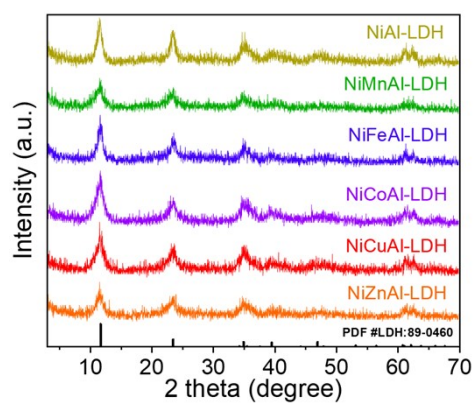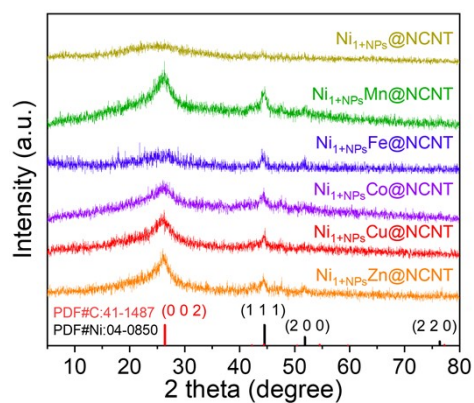
Figure S1. XRD patterns of NiMAl-LDH.

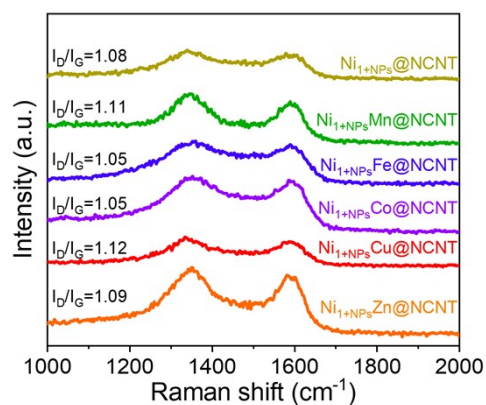Figure S2. XRD patterns of $Ni_{1+NPs}M@NCNTs$.
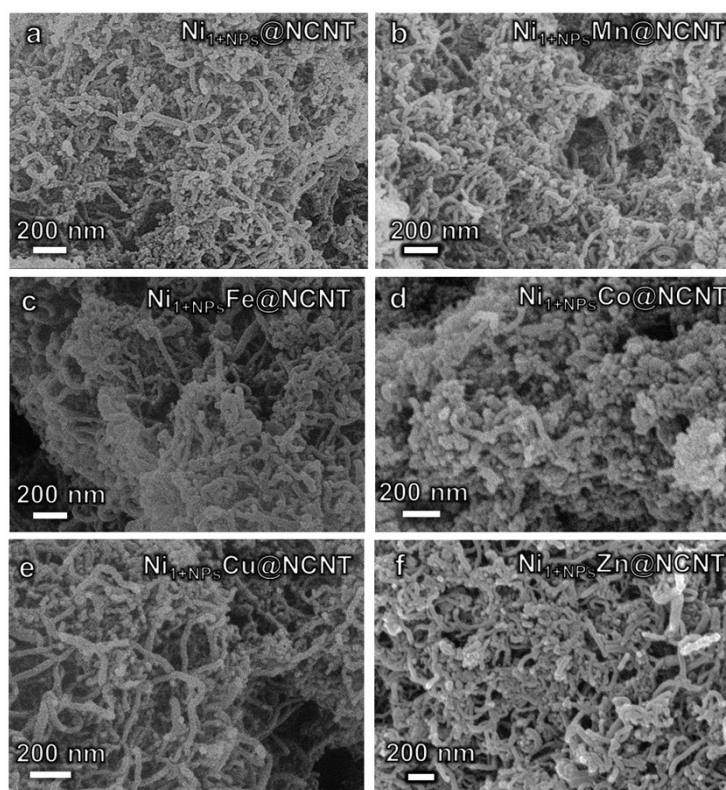

Figure S3. Raman spectra of $Ni_{1+NPs}M@NCNT$.

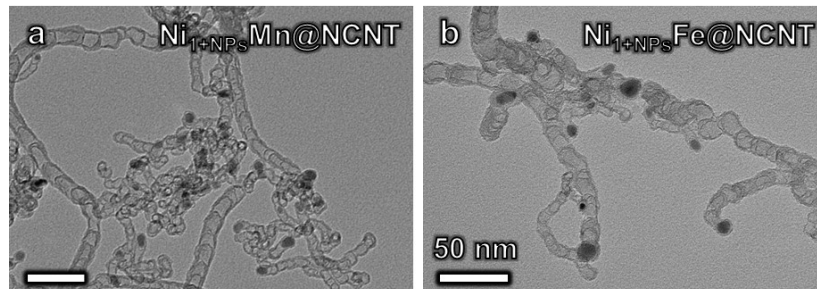Figure S4. (a-f) SEM images of $Ni_{1+NPs}M@NCNT$ (M=Mn, Fe, Co, Ni, Cu, Zn).

Figure S5. TEM images of (a) $Ni_{1+NPs}Mn@NCNT$ and (b) $Ni_{1+NPs}Fe@NCNT$.
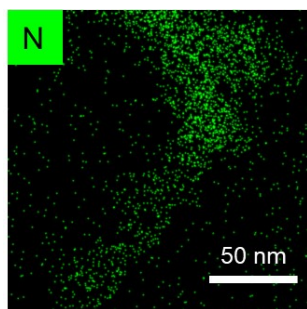
Figure S6. EDX elemental mapping image of N in the $Ni_{1+NPs}Cu@NCNT$.
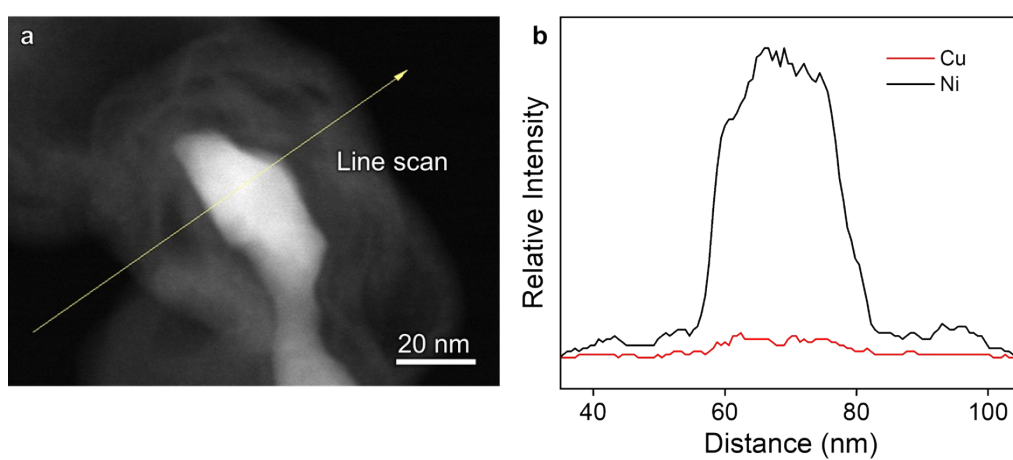

Figure S7. (a) STEM image of $Ni_{1+NPs}Cu@NCNT$ and (b) the corresponding STEM-EDX line scanning image.

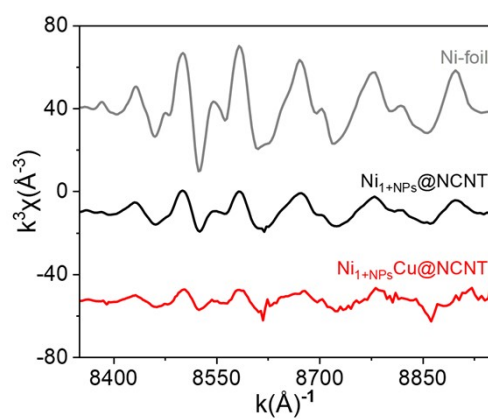Figure S8. EXAFS in k space of Ni$_{1+NPs}$@NCNT, Ni$_{1+NPs}$Cu@NCNT and Ni foil.
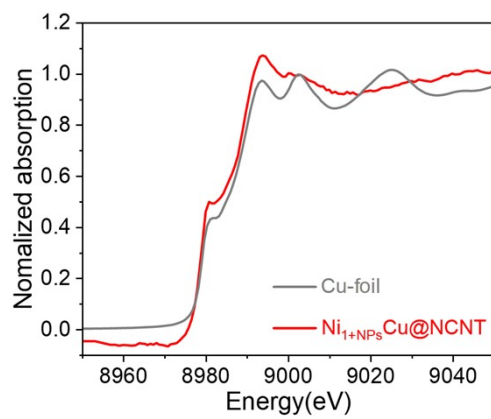

Figure S9. Cu K-edge XANES spectra of Ni$_{1+NPs}$Cu@NCNT and Cu foil
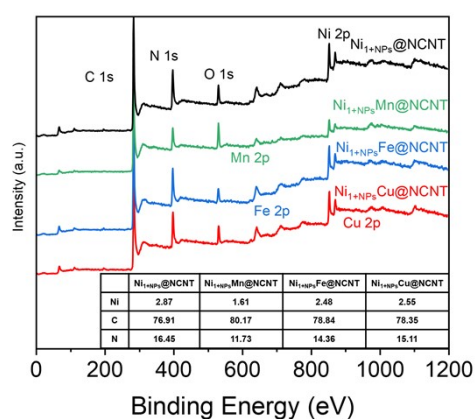
Figure S10. XPS of Ni$_{1+NPs}$@NCNT, Ni$_{1+NPs}$Mn@NCNT, Ni$_{1+NPs}$Fe@NCNT and Ni$_{1+NPs}$Cu@NCNT.
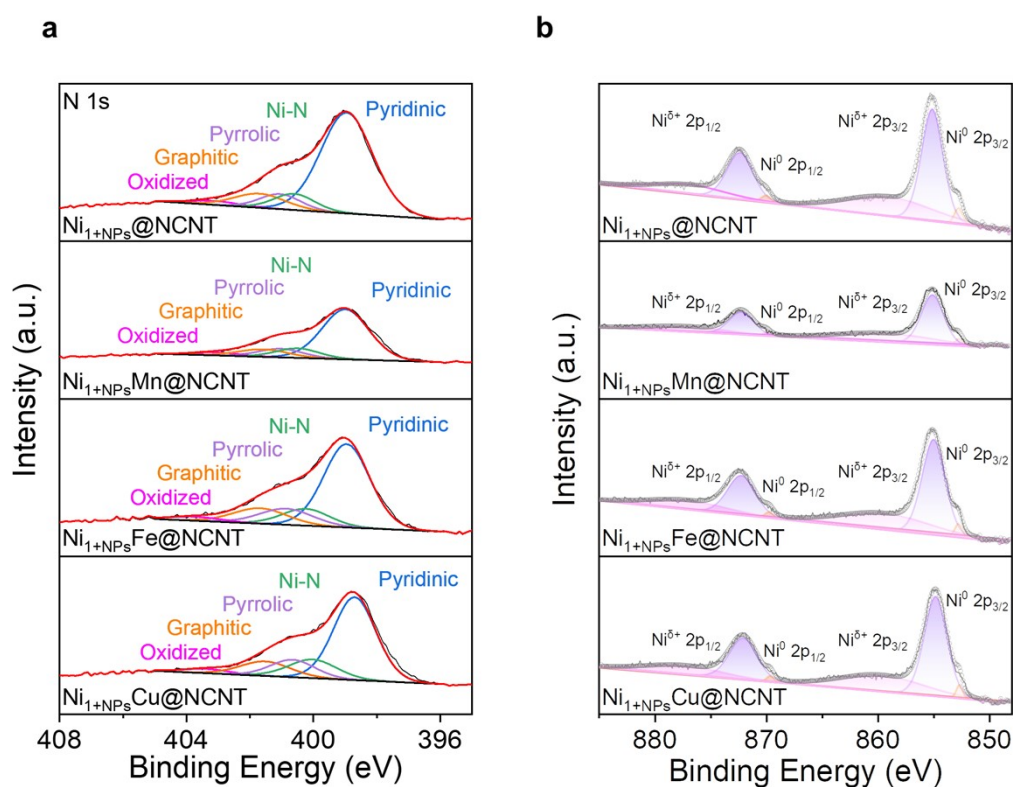

Figure S11. (a) N 1s and (b) Ni 2p XPS spectra of Ni$_{1+NPs}$@NCNT, Ni$_{1+NPs}$Mn@NCNT, Ni$_{1+NPs}$Fe@NCNT and Ni$_{1+NPs}$Cu@NCNT.

Table S1. EXAFS fitting results of $Ni_{1+NPs}Cu@NCNT$, $Ni_{1+NPs}@NCNT$ and Ni foil.

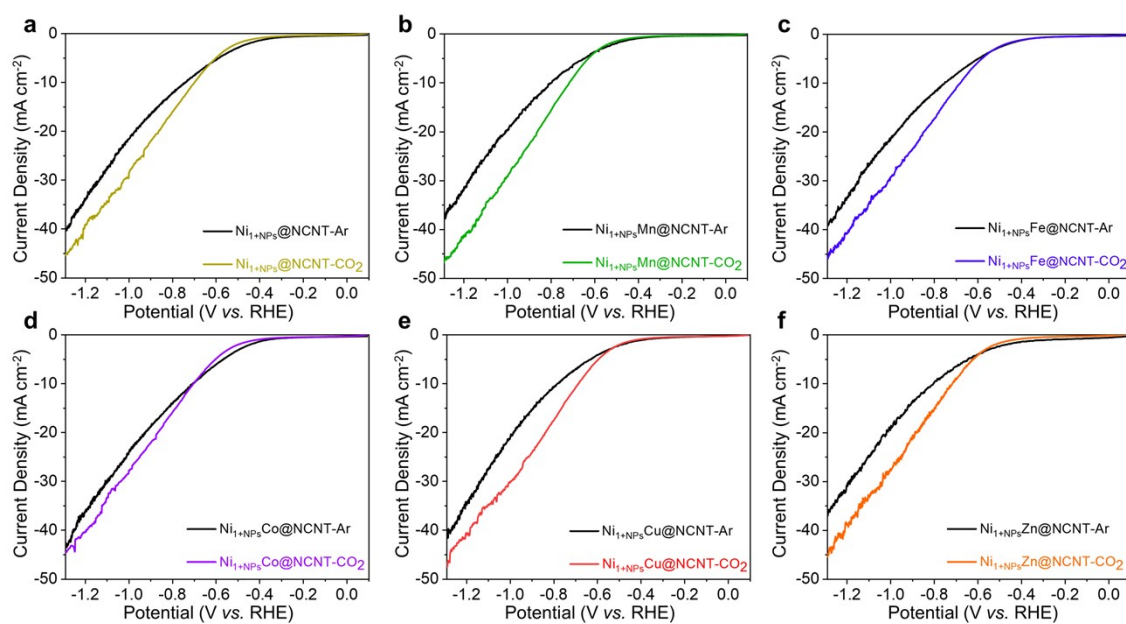| Sample	shell	C.N.	R (Å)	$\Delta\sigma^2 (/10^{-3}Å^2)$	$\Delta E_0(eV)$	R factors
Ni-foil	Ni-Ni	12	2.48	5.83	-5.85	0.0010
$Ni_{1+NPs}@NCNT$	Ni-N	3.96	1.81	14.00	-7.00	0.0027
	Ni-Ni	2.15	2.49	5.06	-4.77	
$Ni_{1+NPs}Cu@NCNT$	Ni-N	3.91	1.81	19.00	-5.00	0.0195
	Ni-Ni	0.88	2.49	3.36	-4.85	

Figure S12. (a-f) LSV curves of $Ni_{1+NPs}M@NCNT$ under Ar (black) and CO_2 (colored) atmosphere.
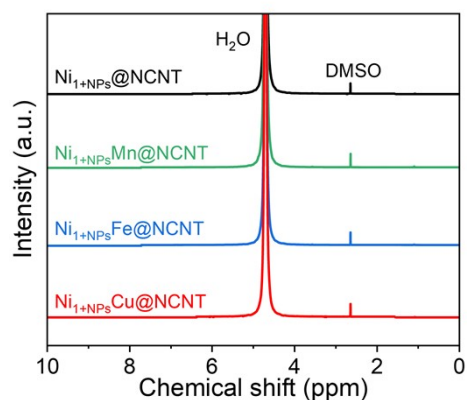
Figure S13. Characterization for the liquid product of $Ni_{1+NPs}M@NCNT$ after the full-potential-CO_2RR period by ^1H nuclear magnetic resonance spectroscopy.

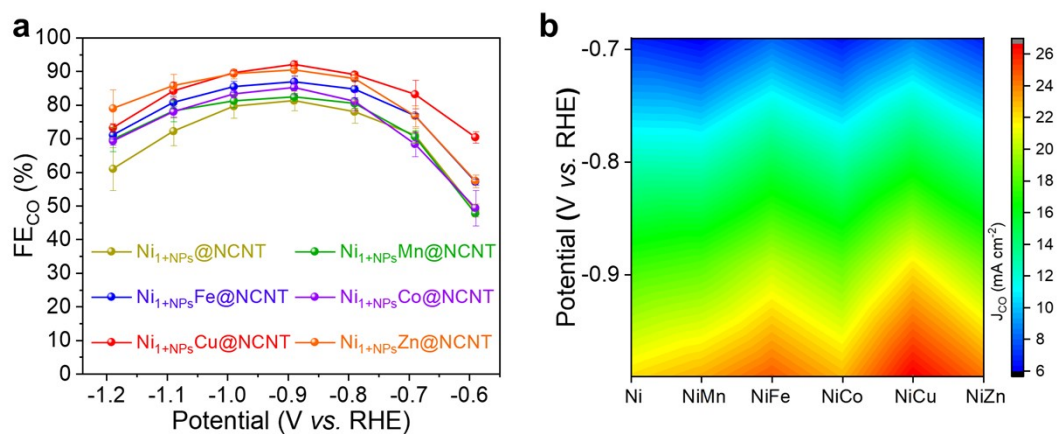Figure S14. CO_2RR performance of $Ni_{1+NPs}M@NCNT$. (a) FE_{CO} of $Ni_{1+NPs}M@NCNT$ (M=Mn, Fe, Co, Ni, Cu, Zn); (b) contour plots of J_{CO} under different potential.

Table S2. FE_{CO} of $Ni_{1+NPs}M@NCNT$ under different potentials.

Potential (V vs. RHE)	$Ni_{1+NPs}@NCNT$	$Ni_{1+NPs}Mn@NCNT$	$Ni_{1+NPs}Fe@NCNT$	$Ni_{1+NPs}Co@NCNT$	$Ni_{1+NPs}Cu@NCNT$	$Ni_{1+NPs}Zn@NCNT$
-0.59	48.64	47.64	57.15	49.34	70.37	57.40
-0.69	70.99	70.51	76.81	68.34	83.15	76.73
-0.79	77.96	80.44	84.70	81.07	89.0	87.85
-0.89	81.26	82.37	86.86	85.18	92.06	90.42
-0.99	79.60	81.20	85.44	83.25	89.56	89.27
-1.09	72.16	78.17	80.74	77.96	84.15	85.73
-1.19	60.96	69.72	71.04	69.23	73.18	78.96

Figure S15. Typical cyclic voltammetry curves for (a) Ni_{1+NPs}@NCNT, (b) Ni_{1+NPs}Mn@NCNT, (c) Ni_{1+NPs}Fe@NCNT and (d) Ni_{1+NPs}Cu@NCNT under different scan rates.

Figure S16. (a) XRD patterns of Ni_{1+NPs}Cu@NCNT before (black) and after (red) CO_2RR; (b) TEM image of the Ni_{1+NPs}Cu@NCNT after CO_2RR.

Figure S17. DFT models for Ni_{1+NPs}@NCNT and $Ni_{1+NPs}Cu$@NCNT.

Figure S18. CO$_2$RR performance of Ni_{NPs}@NCNT. (a) current density and (b) FE_{CO} and FE_{H2} under different potentials.

Figure S19. (a) Schematic illustration and (b) photograph of the flow cells.

Figure S20. (a) TCD1 Chromatogram of CO; and (b) TCD2 Chromatogram of H_2.

Table S3. Comparison of CO_2RR performance displayed by our catalyst and other reported works.

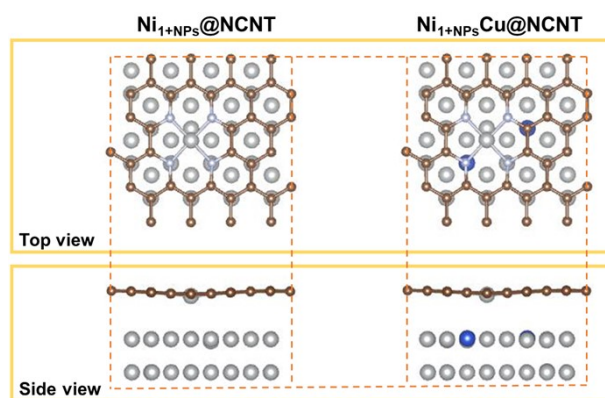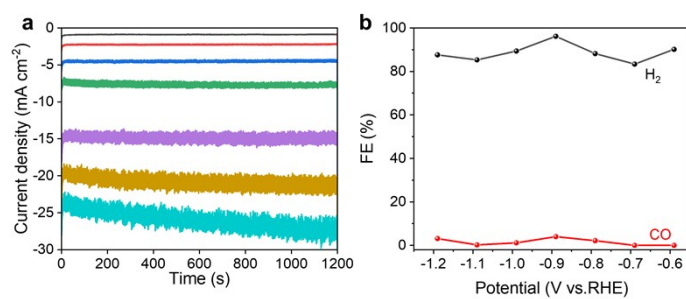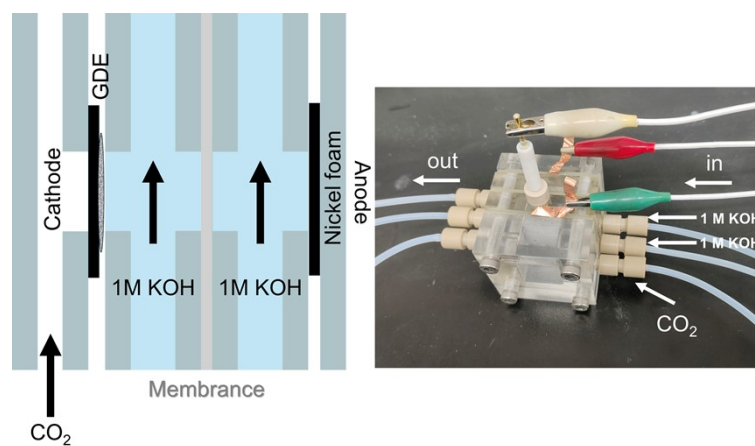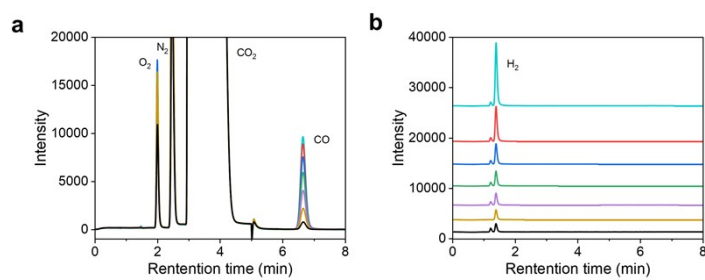| Material	Electrolyte	cell	FE_{CO} (%)	Potential (V vs. RHE)	Current density (mA cm^{-2})	Ref.
ACP/S-N-Ni	0.5 M KHCO$_3$	H-type	91	-0.77	4.1	[9]
Ni SAs/N-C	0.5 M KHCO$_3$	H-type	71.9	-0.9	10.48	[10]
NiSA-N-CNTs	0.5 M KHCO$_3$	H-type	91.3	-0.7	25.74	[11]
Ni-N-C	0.1 M KHCO$_3$	H-type	97	-0.75	7.73	[12]
Ni-N$_3$-C	0.5 M KHCO$_3$	H-type	95.6	-0.65	6.95	[13]
NiN-GS	0.1 M KHCO$_3$	H-type	93.2	at 0.7 V overpotential	4.16	[14]
	1M KHCO$_3$	Flow cell	91.9	at 0.66 V overpotential	10.68	
NiPc-COF	0.5 M KHCO$_3$	H-type	99.1	-0.9 V	-	[15]
	1 M KOH	Flow cell	94.4	-0.5 V	54	
Ni(NC)-1	0.5 M KHCO$_3$	H-type	99	-0.75, -0.80	-	[16]
	1 M KOH	Flow cell	99	-1.82	160	
Ni^I-NCNT @Ni$_9$Cu	0.5 M KHCO$_3$	H-type	97	-0.73	32.87	[17]
Ni$_{1+NPs}$Cu @NCNT	0.25 M KHCO$_3$	H-type	92	-0.89	23.69	This work
	1 M KOH	Flow cell	96.92	-0.78	171.25	

References

1   T.D. Kühne, M. Iannuzzi, M.D. Ben, V.V. Rybkin, P. Seewald, F. Stein, T. Laino, R.Z. Khaliullin, O. Schütt, F. Schiffmann, D. Golze, J. Wilhelm, S. Chulkov, M.H. Bani-Hashemian, V. Weber, U. Borštnik, M. Taillefumier, A.S. Jakobovits, A. Lazzaro, H. Pabst, T. Müller, R. Schade, M. Guidon, S. Andermatt, N. Holmberg, G.K. Schenter, A. Hehn, A. Bussy, F. Belleflamme, G. Tabacchi, A. Glöß, M. Lass, I. Bethune, C.J. Mundy, C. Plessl, M. Watkins, J. VandeVondele, M. Krack, J. Hutter, CP2K: An electronic structure and molecular dynamics software package - Quickstep: Efficient and accurate electronic structure calculations, *J. Chem. Phys.*, 2020, **152**, 194103.

2   J.P. Perdew, K. Burke, M. Ernzerhof, Generalized Gradient Approximation Made Simple, *Phys. Rev. Lett.*, 1996, **77**, 3865.

3   J. VandeVondele, J. Hutter, Gaussian basis sets for accurate calculations on molecular systems in gas and condensed phases, *J. Chem. Phys.*, 2007, **127**, 114105.

4   C. Hartwigsen, S. Goedecker, J. Hutter, Relativistic separable dual-space Gaussian pseudopotentials from H to Rn, *Phys. Rev. B*, 1998, **56**, 3641.

5   S. Grimme, J. Antony, S. Ehrlich, H. Krieg, A consistent and accurate ab initio parametrization of density functional dispersion correction (DFT-D) for the 94 elements H-Pu, *J. Chem. Phys.*, 2010, **132**, 154104.

6   S. Grimme, S. Ehrlich, L. Goerigk, Effect of the damping function in dispersion corrected density functional theory, *J. Comput. Chem.*, 2011, **32**, 1456.

7   T. Lu, F. Chen, Multiwfn: a multifunctional wavefunction analyzer, *J. Comput. Chem.*, 2012, **33**, 580.

8   P. Ros, A.V.D. Avoird, G.C.A. Schuit, Molecular Orbital Calculations on Copper Chloride Complexes, *Coord. Chem. Rev.*, 1967, **2**, 77.

9   S. Li, M. Ceccato, X. Lu, S. Frank, N. Lock, A. Roldan, X.-M. Hu, T. Skrydstrup, K. Daasbjerg, Incorporation of nickel single atoms into carbon paper as self-standing electrocatalyst for CO_2 reduction, *J. Mater. Chem. A*, 2021, **9**(3), 1583-1592.

10   C. Zhao, X. Dai, T. Yao, W. Chen, X. Wang, J. Wang, J. Yang, S. Wei, Y. Wu, Y. Li, Ionic Exchange of Metal-Organic Frameworks to Access Single Nickel Sites for Efficient Electroreduction of CO_2, *J. Am. Chem. Soc.*, 2017, **139**(24), 8078-8081.

11   Y. Cheng, S. Zhao, B. Johannessen, J.P. Veder, M. Saunders, M.R. Rowles, M. Cheng, C. Liu, M.F. Chisholm, R. De Marco, H.M. Cheng, S.Z. Yang, S.P. Jiang, Atomically Dispersed Transition Metals on Carbon Nanotubes with Ultrahigh Loading for Selective Electrochemical Carbon Dioxide Reduction, *Adv. Mater.*, 2018, **30**(13), 1706287.

12   F. Pan, H. Zhang, Z. Liu, D. Cullen, K. Liu, K. More, G. Wu, G. Wang, Y. Li, Atomic-level active sites of efficient imidazolate framework-derived nickel catalysts for CO_2 reduction, *J. Mater. Chem. A*, 2019, **7**(46), 26231-26237.

13   Y. Zhang, L. Jiao, W. Yang, C. Xie, H.L. Jiang, Rational Fabrication of Low-Coordinate Single-Atom Ni Electrocatalysts by MOFs for Highly Selective CO_2 Reduction, *Angew. Chem. Int. Ed.*, 2021, **60**(14), 7607-7611.

14   K. Jiang, S. Siahrostami, A.J. Akey, Y. Li, Z. Lu, J. Lattimer, Y. Hu, C. Stokes, M. Gangishetty, G. Chen, Y. Zhou, W. Hill, W.-B. Cai, D. Bell, K. Chan, J.K. Nørskov, Y. Cui, H. Wang, Transition-Metal Single Atoms in a Graphene Shell as Active Centers for Highly Efficient Artificial Photosynthesis, *Chem*, 2017, **3**(6), 950-960.

15   M.D. Zhang, D.H. Si, J.D. Yi, S.S. Zhao, Y.B. Huang, R. Cao, Conductive Phthalocyanine-Based Covalent Organic Framework for Highly Efficient Electroreduction of Carbon Dioxide, *Small*, 2020, **16**(52), 2005254.

16   C.F. Wen, F. Mao, Y. Liu, X.Y. Zhang, H.Q. Fu, L.R. Zheng, P.F. Liu, H.G. Yang, Nitrogen-Stabilized Low-Valent Ni Motifs for Efficient CO_2 Electrocatalysis, *ACS Catal.*, 2019, **10**(2), 1086-1093.

17   T. Zhang, X. Han, H. Yang, A. Han, E. Hu, Y. Li, X.Q. Yang, L. Wang, J. Liu, B. Liu, Atomically Dispersed Nickel(I) on an Alloy-Encapsulated Nitrogen-Doped Carbon Nanotube Array for High-Performance Electrochemical CO_2 Reduction Reaction, *Angew. Chem. Int. Ed.*, 2020, **59**(29), 12055-12061.